Title: Variations of intracellular density during the cell cycle arise from tip-growth regulation in fission yeast

Short title: Density variations during the fission yeast cell cycle

Authors: Pascal D. Odermatt[1,2], Emrah Bostan[3], Kerwyn Casey Huang[2,4,5,*], Fred Chang[1,*]

[1]Department of Cell and Tissue Biology, University of California, San Francisco, San Francisco, CA 94143, USA

[2]Department of Bioengineering, Stanford University, Stanford, CA 94305, USA

[3]Informatics Institute, University of Amsterdam, Amsterdam, Netherlands

[4]Department of Microbiology and Immunology, Stanford University School of Medicine, Stanford, CA 94305, USA

[5]Chan Zuckerberg Biohub, San Francisco, CA 94158

*Contact: kchuang@stanford.edu and fred.chang@ucsf.edu

Keywords: quantitative phase imaging, fission yeast, *Schizosaccharomyces pombe*, dry-mass density, cell-cycle arrest, cytokinesis, mitosis

Abstract

Intracellular density is a critical parameter that impacts the physical nature of the cytoplasm and has the potential to globally affect cellular processes. How density is regulated during cell growth is poorly understood. Here, using a new quantitative phase imaging method, we show that dry-mass density varies during the cell cycle in the fission yeast *Schizosaccharomyces pombe*. Density decreased during G2 phase, increased in mitosis and cytokinesis, and rapidly dropped at cell birth. These density variations can be explained mostly by a constant rate of biomass synthesis throughout the cell cycle, coupled to slowdown of volume growth during mitosis and cytokinesis and rapid expansion post-cytokinesis. Arrest at specific cell-cycle stages led to continued increases or decreases in density. Spatially heterogeneous patterns of density suggested a link between tip growth and density regulation. Density differences between daughter cells in cells delayed in cytokinesis resulted in bending of the septum away from the high-density daughter, suggesting that intracellular density correlates with turgor pressure. Our results demonstrate that the systematic variations in density during the cell cycle are determined predominantly by modulation of volume expansion, and reveal functional consequences of intracellular density gradients.

Introduction

Intracellular density, a cumulative measure of the concentrations of all cellular components, is an important parameter that globally affects cellular function. Density affects the concentration and activities of biomolecules, and can impact biophysical properties of the cytoplasm such as macromolecular crowding, diffusion, mechanical stiffness, and phase transitions[1-4]. Although it is often assumed that density must be maintained at a particular level to optimize fitness, there is a growing appreciation that density often varies across physiological conditions. Substantial shifts in density and/or crowding have been demonstrated in development, aging, and disease states[3]. Even normal cell-cycle progression can involve changes in density; in cultured mammalian cells, volume increases by 10-30% during mitosis[5,6], which likely dilutes the cytoplasm prior to an increase in density during cytokinesis.

The homeostatic mechanisms maintaining cellular density remain poorly understood. Over the course of a typical cell cycle, cells both double their volume and duplicate all cellular contents. A critical unresolved question is how volume growth and biosynthesis are coordinated. In walled cells, the rate of volume growth is dictated largely by cell-wall synthesis and turgor pressure[7]. In principle, feedback mechanisms could exist that tightly couple biosynthesis with wall expansion. However, recent studies demonstrated that it is possible to decouple biosynthesis and volume growth. For instance, budding yeast cells that are arrested in G1 phase grow to very large sizes and exhibit dilution of the cytoplasm accompanied by decreased protein synthesis and growth rate[8]. Conversely, inhibition of volume growth in fission yeast using osmotic oscillations or inhibition of secretion leads to increased density accompanied by a subsequent dramatic increase in volume growth rate[9].

Numerous methods have been developed to measure aspects of biomass and intracellular density and crowding in living cells[10]. Suspended microchannel resonators (SMR) infer buoyant cell mass from changes in the frequency of a resonating cantilever as a single cell passes through an embedded microchannel[11]. Quantitative phase imaging (QPI) is a well-established optical technique for extracting dry-mass measurements from changes in the refractive index[12]. The interpretation of phase shifts depends on the similarity in the refractive indices of major cellular components such as proteins, lipids, and nucleic acids[10]. Previous studies have used phase gratings or holography to generate phase-shift maps that can be used to quantify intracellular density; these approaches require specialized equipment[13].

Here, we develop a new QPI method for measuring the intracellular density of fission yeast cells. This label-free method is based on the analysis of *z*-stacks of brightfield images[14], thus having the advantage of not requiring a specialized phase objective or holographic system. Fission yeast is a leading cell-cycle model, as cells have a highly regular rod-like shape, size, and cell cycle conducive to quantitative analyses. Using QPI, we show that wild-type fission yeast cells exhibit characteristic density changes during the cell cycle, in which density falls during G2 phase and increases during mitosis and cytokinesis. These density variations can be explained by variations in volume growth while mass grows exponentially throughout the cell cycle, and perturbations to cell-cycle progression and/or growth has predictable effects on density. We further describe intracellular density gradients and a correlation of intracellular density with osmotic pressure and envelope mechanics. Our findings illustrate a general mechanism of density regulation through adjusting the relative rates of volume growth and biosynthesis.

Results

Quantitative phase imaging enables high-resolution measurements of intracellular density in growing cells

To measure intracellular density using a standard wide-field microscope, we developed a version of QPI in which the phase shift is retrieved computationally from a *z*-stack of brightfield images[14]. This label-free approach takes advantage of the linear relationship between the intracellular concentration of biomolecules and the refractive index of the cell interior, which can be computed from the light intensity profile along the *z*-direction using the transport-of-intensity equation (Figure 1A, Methods). To calibrate phase shifts with absolute concentrations (dry-mass/volume), we measured the phase shifts within cells in media containing a range of concentrations of bovine serum albumin (BSA) (Methods) and confirmed a linear relationship that can be used to extrapolate the density of cells (Figure 1B). This method provides pixel-scale measurements of density in living cells, and can easily be applied during time-lapse imaging with sub-minute time resolution on most wide-field microscopes. Using this methodology, the mean intracellular density of an asynchronous population of *S. pombe* cells growing at 30 °C in rich YE5S medium was 282±16 mg/mL (Figure 1C). The distribution was remarkably narrow, with coefficient of variation of 0.06, despite variability in cell size, cell-cycle stage, and the various sources of intracellular heterogeneities such as lipid droplets (Figure S1) and cell wall septa (both of which were regions of high signal). The nucleus was not apparent in most phase-shift maps, indicating similar density as the cytoplasm (Figure 1A). A similar distribution of densities was observed in cells grown at 25 °C and after temperature shifts (Figure 1D). These results suggest that dry-mass density is robustly maintained, and demonstrate that this QPI approach

106 can precisely measure absolute dry-mass density in living cells with high temporal and spatial
107 resolution.
108
109 **Intracellular density follows a characteristic trajectory during the cell cycle**
110 To determine whether intracellular density changes over the course of the cell cycle, we imaged
111 proliferating cells in time-lapse using QPI in a microfluidic device under constant flow of growth
112 medium (Methods) (Figure 2A, Movie S1). Density maps were segmented to extract cellular
113 dimensions, from which volume was computed (Figure 1A) (Methods). Total dry mass of each
114 cell was computed from volume and mean density measurements. We imaged cells throughout
115 their entire cell cycle, and then aligned the computed data from each cell by relative cell-cycle
116 progression, from cell birth (first detectable physical separation between daughter cells) until
117 just before cell-cell separation at the end of the cell cycle. As observed previously[15], cells
118 exhibited steady tip growth in interphase (mostly G2 phase), and then volume growth slowed or
119 halted during mitosis and cytokinesis (defined here as the period starting from septum
120 formation and ending at daughter-cell separation) (Figure 2B).
121
122 Intracellular density displayed consistent dynamics during the cell cycle. Density gradually
123 decreased from the beginning of the cell cycle through G2 phase by ~5%, followed by a steady
124 rise in mitosis and cytokinesis (Figure 2C). We confirmed these findings using a complementary
125 approach for measuring density. Holographic imaging (Methods) showed that the mean
126 refractive index of cells decreased with cell length prior to septation, whereas cells of similar
127 length with a septum exhibited higher refractive indices (Figure S3A,B)[16].
128

At the end of cytokinesis, the middle layer of the septum is digested and daughter cells separate. During this 5-10-min period, the septum bulges outward on each side to form the rounded new pole in a physical process driven by turgor pressure[17]. Analysis of individual cells showed a consistent drop in density within a 5-min window around cell separation (Figure 2E, S4A,B); during this period, cell volume suddenly increased by ~5% while density decreased by ~5% (Figure 2E). Thus, density appears to be directly tied to the dynamics of volume expansion.

Our precision measurements of cellular dimensions and intracellular density provide a quantitative characterization of dry-mass dynamics (biosynthesis) throughout the cell cycle. The absolute rate of dry-mass accumulation steadily increased during the cell cycle (Figure 2D), and dry-mass dynamics were more exponential than linear in nature (Figure 2F, Figure S2A). The absolute rate of mass synthesis was therefore higher during mitosis and cytokinesis than at the beginning of the cell cycle, even though the cell slowed in volume growth late in the cycle. Thus, mass production was not tightly coupled to volume growth. These measurements suggest a simple model in which the increase of density in mitosis and cytokinesis arises as consequence of continued mass accumulation when volume growth is halted (Figure 2F).

Cell-cycle perturbations exacerbate cell cycle-dependent density variation

Our data demonstrate that intracellular density increases during mitosis and cytokinesis because biosynthesis continues unabated while volume growth slows down; conversely, density decreases during interphase because the rate of volume growth surpasses the rate of mass synthesis. One possibility is that the relative rate of mass synthesis is not directly coupled to cell-cycle stage-specific volume growth rates, but rather determined by environmental factors; density variations then arise simply as a consequence of cell-cycle regulation of volume

153 expansion, which is controlled by cell polarity programs that redirect the cell envelope growth
154 machinery to the middle of the cell for septum formation prior to cytokinesis[18-20]. Alternatively,
155 the density at each cell-cycle stage could be directly programmed to specific levels by specific
156 cell-cycle regulators. To distinguish these models, we examined the consequences of arresting or
157 delaying cells at particular stages of the cell cycle (Figure 3A). If there is no strict control of
158 biosynthesis, then when mitosis or cytokinesis is blocked, mass should continue to accumulate
159 and density should reach higher levels than in normal cells, and conversely density should fall
160 below normal in extended interphase. If density is instead set at specific levels according to cell-
161 cycle phase, density levels should not change during cell-cycle delays beyond the ranges
162 appropriate for each phase.
163
164 First, we tested whether density would decrease further in cells with an extended period of
165 growth during interphase. We delayed cells in G2 phase using a *cdc25-22* mutant[21] by shifting
166 them from room temperature to the semi-permissive temperature (32 °C) (Figure 3B,C). These
167 cells continued to grow from their tips and formed abnormally elongated cells. To focus on cells
168 that remained in G2 for an extended interval, we limited our analysis to cells that elongated to
169 >2.5-fold their initial length. In these cells, during their prolonged G2 phase of 2-3 h, density
170 decreased further than in wild-type cells (~8% in *cdc25-22* cells from 267±19 to 245±6 mg/mL,
171 compared to ~5% in wild-type cells from 267±11 to 250±6 mg/mL) (Figure 3C). These data
172 suggest that density falls during G2 phase because the rate of volume growth continues to be
173 slightly faster than the rate of biosynthesis.
174
175 Second, we tested whether cells arrested in mitosis would increase in density (Figure 4A). We
176 delayed cells in metaphase using a *cut7-ts* mutant (kinesin-5) defective in mitotic spindle

assembly[22]. We tracked intracellular density from mitosis initiation until the earliest signs of septum formation. As expected, at the non-permissive temperature this interval was longer for *cut7-ts* cells (20-30 min) compared with 10-20 min in wild-type cells (Figure 4B,C). During this mitotic period, the density of wild-type and *cut7-ts* cells increased at a similar rate, hence the extended time in metaphase in *cut7-ts* cells led to a greater density increase (7% in *cut7-ts* from 270±12 to 288±14 mg/mL versus 5% in wild-type cells from 264±11 to 278±13 mg/mL).

Third, we arrested cells in cytokinesis, again to test for an increase in density (Figure 4A). *cdc16-116* mutant cells do not separate, and hence proceed to repeatedly make septa without elongating[23]. Upon a shift from 25 °C to the non-permissive temperature (34 °C), cells that maintained a cytokinetic arrest continued to increase in cytoplasmic density; density after 90 min was 20-30% higher than in cytokinesis-competent wild-type cells (Figure 4D,E). Thus, biosynthesis continues throughout an extended block of mitosis or cytokinesis, leading to abnormally high intracellular density.

Finally, we asked whether inhibition of volume growth is sufficient to increase cytoplasmic density. We previously showed that two treatments that slow down volume growth (osmotic oscillations and treatment with brefeldin A) lead to an increase in cytoplasmic density[9]. However, since these treatments do not completely halt volume growth and/or result in cell death, we treated cells with the F-actin inhibitor latrunculin A, which causes immediate cessation of tip growth independent of cell-cycle stage[24,25]. All latrunculin A-treated cells completely halted tip growth and began to steadily increase in density, regardless of their cell-cycle stage (Figure 6A). The mean density increase after 1 h was ~20% (Figure 6B). Similar increases were seen in cells of different sizes (Figure S5). However, we noted that in contrast to the mitotic and

cytokinesis arrests, mass increases were variable and on average increased more slowly during latrunculin A treatment than during normal growth (Figure S5, Figure 6A), suggesting a partial slowdown in biosynthesis or increase in degradation.

These results indicate that density levels are not coupled to specific cell cycle stages but are sensitive to the regulation of volume growth, and inhibition of volume growth is sufficient to increase intracellular density.

A polarized density gradient is associated with the pattern of tip growth

Fission yeast have a well-known pattern of growth in which after cell division, the old end grows initially, until part-way through G2 phase the new end begins to grow, at a slower rate than the old end[15]. As expected, our time-lapse data showed that the old and new ends grew on average by ~4 and 2 μm, respectively, during the cell cycle. We noted that many cells exhibited a gradient of intracellular density in which the ends that were actively growing appeared less dense than the non-growing ends (Figure 6A). We hypothesized that these subcellular gradients reflected differences in tip growth between the two ends of the cell. In agreement with our hypothesis, the slower-growing new end typically appeared more dense than the faster-growing end. In some cells, the difference in densities between the fast- and slow-growing ends was ~10% of the mean overall density (Figure 6A). The mean density difference between the two ends throughout the cell cycle was ~15 mg/mL, corresponding to ~5% of the mean overall density (Figure 6B). To address the potential for differences in the widths (and hence heights above the coverslip) of old and new ends to influence phase shifts, we constrained our analysis to cells within a narrow range of widths and found that local density and tip growth remained highly correlated (Figure S6A,B). Moreover, in cells treated with latrunculin A to inhibit growth, spatial density gradients

persisted over time (Figure S6C). These results demonstrate that intracellular density is linked to local growth patterns.

Daughter cells directly after cytokinesis often exhibited differences in intracellular density. Time-lapse imaging showed that the intracellular density differences established during interphase were often propagated through cell division and correlated with density differences between the progeny daughter cells after cytokinesis (Figure 6D,E). Thus, subcellular density variations are sufficiently stable to be propagated through generations.

Cell density differences impact septum shape through correlation with turgor pressure

Next, we ascertained whether density differences of the magnitude seen within and across cells with normal physiology (5-20%) have physiological consequences. One possible effect of intracellular density is macromolecular crowding. High concentrations of macromolecules are predicted to produce colloid osmotic pressure that may influence cell mechanics[2]. Consistent with the presence of intracellular gradients in non-septated cells, we observed in septated cells that the densities of daughter compartments were often different (particularly those with delayed cell separation such as *mid1*, *mid2*, and *cdc16* cells), and that the septum between these daughter cells bent away from the more dense compartment (Figure S7). Previous studies showed that the septum is an elastic structure that can be used as a biosensor that informs on osmotic pressure differences between the compartments. For instance, when one daughter is lysed by laser microsurgery and loses turgor pressure, the septum bulges away from the intact daughter[17]. Temporal fluctuations in septum bending thus suggest that the pressure difference between daughter cells alternates in sign[26].

To investigate the relationship between density differences and septum bending, we focused on *mid2Δ* cells. Mid2 is an anillin orthologue that regulates septins in late cytokinesis; *mid2Δ* mutants exhibit long delays (1-2 h) in cell separation and thus most cells in the population have one or more septa[27]. We used QPI imaging to track density over time, and identified the time after septum formation at which the maximum density difference was reached for each cell. 71% (64/90) of cells exhibited a bent septum, and of these cells 97% (62/64) exhibited a septum bent away from the compartment of higher density at the time of maximum density difference (Figure 7A), with a mean maximum difference of 16±5% (Figure 7B). In two cases (2/90), the septum was bent in the opposite manner toward the compartment of lower density. In these cells the maximum density difference was substantially lower (5%; Figure 7B), and may represent septa that fluctuated in direction. Indeed, in one cell the fluctuating direction of septum bending correlated with alternation of the sign of the density difference between the daughter cells (Figure 7C). In instances where the septum appeared flat, the density difference was significantly lower (~4.5%) than in cells with a bent septum.

We also noted density variations and bent septa in multi-septated *mid2Δ* cells. In particular, internal compartments bounded by two septa were hampered in their ability to grow in volume and correspondingly exhibited higher density than the surrounding compartments. These situations were frequently associated with both septa bending away from the higher-density compartment (Figure S7C). The observation that septal bending occurred for density differences as low as 5-10% suggests that the density variations over the course of a normal cell cycle (Figure 2) or between growing and non-growing cell tips (Figure 6) may reflect substantial changes in turgor-mediated stresses.

Discussion

Here, we establish a QPI method based on *z*-stacks of brightfield images for quantifying intracellular density dynamics without specialized equipment. We show that exponential-phase fission yeast cells have a dry mass density of 282±16 mg/mL, comparable to measurements in other organisms[3,28]. Density varied systematically across the cell cycle in wild-type fission yeast cells over a range of ~10%, while the relative rate of dry-mass synthesis remained constant (reflecting exponential accumulation) throughout all cell-cycle stages (Figure 2). These quantitative findings, which utilize precise sub-pixel measurements of cellular dimensions and automated analysis platforms, are consistent with more qualitative density studies of fission yeast using other methods[16,29,30].

Our data support a model in which density variations are a product of programmed changes in volume growth accompanied by a constant relative rate of mass biosynthesis. As a result, volume growth and biosynthesis were not tightly coupled throughout the cell cycle. During tip growth in G2, density dropped steadily (Figure 2C), indicating that the rate of volume growth outpaces biosynthesis during interphase. Density steadily rose during mitosis and cytokinesis (Figure 2C), when volume growth ceases or slows down. After separation of daughter cells (cell birth), density dropped during the rapid increase in cell volume as the new cell poles expanded (Figure 2E), possibly due to water influx. Despite these changes in growth rate and density, it is remarkable that even without tight feedback controls, cells maintained a relatively tight distribution of densities across the population (Figure 1C).

Consistent with this model, density shifts were exacerbated by perturbations of cell-cycle progression or of volume growth directly. *cdc25* mutants delayed at the G2/M transition

exhibited a steady decline in density as cells elongated abnormally, reminiscent of the cytoplasmic dilution observed in very enlarged budding yeast and senescent mammalian cells[8]. During mitotic arrest at the spindle checkpoint (*cut7*) or cytokinesis arrest through regulation of the SIN pathway (*cdc16*), volume growth was slowed but mass synthesis was unaffected, resulting in steady density increases. Inhibition of cell growth with latrunculin A caused a steady increase in density regardless of cell cycle stage. These findings suggest that any perturbation that affects cell-cycle progression or growth will necessarily alter density dynamics. Cell-cycle arrests are commonly used to synchronize cells, and are often triggered in response to stresses such as DNA damage. Our study demonstrates that such perturbations are not as innocuous as often thought; arrests not only affect cell-cycle progression and cell size, but also cause changes in intracellular density.

Our studies provide quantitative measurements of the mass dynamics of individual fission yeast cells throughout the cell cycle. We found that it continued without any apparent change, consistent with previous studies[29,30]. In fact, mass dynamics were exponential in nature, consistent with findings in other cell types[31]. Intriguingly, studies of density and growth in other cell types showed somewhat different cell-cycle patterns. In budding yeast, buoyant density is lowest in early G1 and rises in late G1 and S phase at the time of bud formation[28]. Moreover, cell-cycle arrests in S and M phase and latrunculin A treatment do not lead to increases in buoyant density, unlike our findings in fission yeast. In human cells, mass growth continues in early mitosis, but stops in metaphase and resumes in late cytokinesis, potentially with subtle oscillations[32,33]. Density is constant during much of the cell cycle, but decreases in mitosis (by 0.5% in buoyant mass, equivalent to >10% decrease in dry-mass density) coincident with a 10-30% volume increase during mitotic rounding; density then slightly increases in cytokinesis[5,6]. In

the bacterium *Escherichia coli*, density varies somewhat from birth to division, but the ratio of surface area to mass is relatively constant, suggesting that biosynthesis is linked to surface area synthesis[34]. We found that in fission yeast, mass was also more closely coupled with surface area than volume, especially when including the surface area of both sides of the septum (Figure S2B-D), although mass continued to accumulate during latrunculin A treatment despite minimal (if any) surface area growth (Figure 5B). It remains to be seen what general rules of cell density regulation will emerge from comparisons across organisms.

Our findings also provide insight into the relationship between the rate of volume growth and subcellular density regulation. Fission yeast cells grow through tip growth, which involves the extension and assembly of new cell wall and plasma membrane, which are accomplished by a complex integration of the cell-polarity machinery, exocytosis, wall growth and mechanics, and turgor pressure. In addition to the global effect of volume growth on density, the intriguing polarization of density patterns (Figure 6) suggests that tip growth influences local intracellular density patterns more directly. Spatial gradients revealed that local density was correlated with tip growth (Figure 6C), with slow-growing ends having higher density. It is not yet clear what cellular components are responsible for this spatial pattern, and whether they are actively depleted at growing cell tips or concentrated at non-growing regions. The relevant components may be membrane-bound or membrane-less organelles; it is unlikely that they are soluble, freely diffusing particles, unless a diffusion barrier (perhaps the nucleus) exists. Polarized density patterns established in interphase were often propagated through cell division and appeared to be inherited by the daughter cells, resulting in density differences across a lineage. How these patterns may lead to asymmetrical behaviors in cell lineages remain to be explored.

Effects of intracellular density changes on cellular functions are only beginning to be appreciated. Density changes of 5-20%, which likely affect the concentration of most if not all cellular components in the cytoplasm, could have profound consequences for the biochemistry of cellular reactions and on macromolecular crowding. Here we revealed that density also effects cell mechanics. Intracellular osmotic pressure and density differences between daughter compartments were highly correlated, as evidenced by bending of the elastic septal cell wall. Macromolecular crowding is thought to produce colloid osmotic pressure, which has been proposed to influence nuclear size control[2,35]. Our data suggests that density-dependent colloid pressure differences globally affect fission yeast cells by changing the distribution of mechanical stresses within the cell wall.

Another possible consequence of intracellular density changes is regulation of volume expansion. In fission yeast, perturbations that increase density are accompanied by a subsequent dramatic increase in volume growth rate that persists for hours[9]. Such growth regulation may play an important role in density homeostasis. Taken together, we speculate that the increase of density at cell division both may provide mechanical force through increased turgor pressure to facilitate cell-cell separation and bulging of the cell wall[17], and perhaps to accelerate tip growth in the newly born cell[9]. Future studies focusing on the effects of cell density on particular cellular processes will be needed to understand the full scope of these density changes.

Methods

Strains and cell culturing

All strains used in this study are listed in Table S1. In general, cultures were grown in 3 mL of YES medium at 30 °C on a rotating shaker overnight to an OD_{600}~1, diluted to OD_{600}~0.1, and incubated until OD_{600}~0.3 for imaging. Temperature sensitive mutant c*dc25-22* cells (and wild-type control cells) were first grown at room temperature, and 90 min after imaging started temperature was increased to 32 °C. Temperature sensitive mutant *cdc16-116* cells (and wild-type control cells) were first grown at 25 °C, and then imaged on the microscope with the temperature controlled enclosure pre-heated to 34 °C. Temperature sensitive mutant *cut7-446* cells (and wild-type control cells) were first grown at 25 °C, then imaged on the microscope with the temperature controlled enclosure pre-heated to 30 °C.

Single-cell imaging

Images were acquired with a Ti-Eclipse inverted microscope (Nikon) equipped with a 680-nm bandpass filter (D680/30, Chroma Technology) in the illumination path with a 60X (NA: 1.4) DIC oil objective (Nikon). Before imaging, Koehler illumination was configured and the peak illumination intensity at 10-ms exposure time was set to the middle of the dynamic range of the Zyla sCMOS 4.2 camera (Andor Technology). mManager v. 1.41[36] was used to automate acquisition of *z*-stack brightfield images with a step size of 250 nm from ±3 μm around the focal plane (total of 25 imaging planes) to ensure substantial oversampling that facilitated correcting for potential drift in the *z*-direction over the course of each experiment at 5 or 10 min intervals at multiple x/y-positions.

Microfluidics

Cellasic microfluidic flow cell plates (Millipore, Y04C) controlled by a ONIX or ONIX2 (Millipore) microfluidic pump system were used for imaging. YES medium was loaded into all but one of the fluid reservoirs; the remaining well was loaded with 100 mg/mL bovine serum albumin (BSA) (Sigma Aldrich) solution in YES. Liquid was flowed from all 6 channels for at least 5 min at 5 psi (corresponding to 34.5 kPa), followed by 5 min of flow from YES-containing wells to wash out buffer and fill channels and imaging chambers. The plate was kept in a temperature-controlled enclosure (OkoLab) throughout loading. Cells were then transferred into the appropriate well and loaded into the microfluidic imaging chamber such that a small number of cells were initially trapped, and flow of YES was applied. To ensure full exchange of liquid in the chamber during imaging, flow channel was switched at least 40 s before images were acquired. Every ~2 h, BSA flow was activated during one time point of imaging to calibrate QPI measurements.

Image analysis to retrieve phase shifts

To reduce post-processing time, each *z*-stack was cropped to a square region containing the cell(s) of interest and a border of at least 40 pixels, and the focal plane was identified. This cropping was accomplished by first using FIJI to identify regions of interest (ROIs) within a thresholded standard deviation *z*-projection image of each brightfield *z*-stack. Using Matlab (Mathworks), images were cropped to the ROIs and the standard deviation of the pixels in each ROI was computed. The focal plane was defined based on the image in the stack with the lowest standard deviation. Three images above and three images below the focal plane separated by 500 nm were used to quantify cytoplasmic density. Based on these images, the phase information was calculated using a custom Matlab script implementing a previously published algorithm[14]. In brief, this method relates the phase information of the cell to brightfield image intensity changes

411 along the *z*-direction. Equidistant, out-of-focus images above and below the focal plane are used
412 to estimate intensity changes at various defocus distances. A phase-shift map is reconstructed in
413 a non-linear, iterative fashion to solve the transport-of-intensity equation.
414
415 **Cytoplasmic density quantification**
416 Using Matlab, images were background-corrected by fitting a Gaussian to the highest peak of the
417 histogram (corresponding to the background pixels) of the phase-shift map, and shifting every
418 pixel to shift the background peak to the intensity value corresponding to zero phase shift. These
419 background-corrected phase-shift maps were converted into binary images using watershedding
420 for cell segmentation; where necessary, binary images were corrected manually to ensure
421 accurate segmentation. Binary images were segmented using Morphometrics[37] to generate
422 subpixel-resolved cell outlines.
423
424 Each cell outline was skeletonized using custom Matlab code as follows. First, the closest-fitting
425 rectangle around each cell was used to define the long axis of the cell. Perpendicular to the long
426 axis, sectioning lines at 250-nm intervals and their intersection with the cell contour were
427 computed. The centerline was then updated to run through the midpoint of each sectioning line
428 between the two contour-intersection points. The slope of each sectioning line was then updated
429 to be perpendicular to the slope of the centerline around the midpoint. Sectioning lines that
430 crossed a neighboring line were removed. Cell volume and surface area were calculated by
431 summing the volume or area of each section assuming rotational symmetry. Volume and area of
432 the poles were calculated assuming a regular spherical cap.
433

To convert the mean intensity of the phase-shift within each cell into absolute concentration (in units of mg/mL), the mean of all cells across all time points was first calculated. Then, the decrease in phase shift induced by a prescribed concentration of BSA (typically 100 mg/mL) was defined as the difference between the mean of the phase shifts before and after the BSA imaging time point and the phase shift during the BSA time point. This difference in intensity established the calibration scaling between phase shift intensity and the concentration of BSA (Figure 1B). The cytoplasmic density of each cell was then calculated by dividing the mean phase shift of the cell by the aforementioned scaling factor. The mass of each cell was inferred from its mean density and volume.

BSA calibration

Channel slides (µ-Slide VI 0.4, ibidi) were coated with lectin (Sigma-Aldrich, L1395) (0.1 mg/mL in water) for ~5 min, washed with YES, and cells were added and incubated for ~5 min to allow for attachment. Loose cells were removed by washing with YES. Attached cells were first imaged in YES medium. BSA was then added to a final concentration of 200 mg/mL. Consecutively, YES was added to dilute BSA to the desired concentrations (150, 100, and 50 mg/mL), followed by washout of the BSA and imaging in YES.

BODIPY staining and imaging

10 µL aliquots of 100 mM BODIPY 493/503 (Thermo Fisher, D3922) in absolute ethanol were prepared. Ethanol was then evaporated in a desiccator under vacuum and dried aliquots stored at 4 °C for long term storage. Before use, an aliquot was redissolved in 10 µL absolute ethanol and to cells in YES 1 µL was added per cell density OD_{600} of 0.1. The cell-dye mix was incubated protected from light for ~1 min at room. Cells were then pelleted at 2000 rpm for 1 min and

458 medium was exchanged with fresh YES. Cells were spotted onto agarose pads and imaged with
459 an EM-CCD camera (Hamamatsu) through a spinning-disk confocal system (Yokogawa CSU-10)
460 attached to one of the ports of the Ti-Eclipse inverted microscope with a 488 nm laser. In
461 parallel, brightfield *z*-stack images were acquired for QPI analysis.
462
463 **Lineage tracking for time-lapse imaging datasets**
464 First, each cell present at the beginning of the experiment was linked to the closest cell in the
465 next frame based on the distance between centers and the difference in their size (crossectional
466 area). A cell was considered the same if the centers between consecutive time points was within
467 20 px (~2μm) and the cross-sectional area was not smaller than 70% compared to the previous
468 time point. This process was iterated to define the lineage until either requirement was violated
469 (usually occurring during cell division), at which point a new lineage was initialized using the
470 earliest unassigned cell. All lineages were visually inspected and corrected when necessary.
471
472 **Polar growth and density quantification**
473 To separately quantify the growth of the new and old pole, fiduciary markers such as birth scars
474 on the cell outline were identified from which the distance to each pole at the beginning and end
475 of the cell cycle was measured. The density of each polar region was calculated by extracting the
476 peak of the histogram of density values in the region within 3 μm of the pole at each time point,
477 and then calculating the mean over time points.
478
479 **Holographic refractive index measurements**
480 For refractive index measurements, wild-type cells grown at 30 °C were immobilized on a lectin-
481 coated glass-bottom 35 mm diameter μ-dish (ibidi). Holographic refractive index measurements

were acquired with a 3D Cell Explorer system (Nanolive) with a temperature-controlled enclosure set to 30 °C. First, sum images of *z*-stacks of three-dimensional refractive index maps were generated to retrieve cell outlines by watershedding. Cells oriented at an angle to the flat glass bottom dish were ignored. For each remaining cell, the mean refractive index was extracted from each image in the *z*-stack using Matlab and the highest value (assumed to correspond to the middle plane) was used for further analysis.

Latrunculin A treatment

Stock solutions were made by dissolving 100 µg latrunculin A (Abacam, ab144290) in DMSO (Sigma-Aldrich) to a concentration of 20 mM and stored at -20 °C in 1 µL aliquots. To prepare agarose pads, 1 µL of 20 mM latrunculin A or 1 µL of DMSO was mixed with 100 µL of YES medium containing 2% w/v agarose UltraPure agarose (Invitrogen Corporation, Carlsbad, CA, USA) kept in a water bath at ~70 °C. The mixture was pipetted onto a microscope glass slide and quickly covered with another slide to form flat agarose pads with thickness of ~2 mm. Once pads had solidified, one slide was carefully removed and 1-2 µL of exponential-phase wild-type cells were deposited on the agarose pad. Cells were allowed to settle for 1-2 min before a coverslip was placed on top and sides were sealed with Valap (1:1:1 vaseline:lanolin:paraffin) to prevent evaporation during imaging.

Acknowledgements

We thank the Chang and Huang labs for discussion and support, to Gabriella Estevam for contributions early in the project. P.D.O. was supported by postdoctoral fellowships from the Swiss National Science Foundation under Grants P2ELP3_172318 & P400PB_180872. F.C. was supported by NIH GM056836. K.C.H. is a Chan Zuckerberg Biohub investigator.

References

1 van den Berg, J., Boersma, A. J. & Poolman, B. Microorganisms maintain crowding homeostasis. *Nat Rev Microbiol* **15**, 309-318, doi:10.1038/nrmicro.2017.17 (2017).

2 Mitchison, T. J. Colloid osmotic parameterization and measurement of subcellular crowding. *Mol Biol Cell* **30**, 173-180, doi:10.1091/mbc.E18-09-0549 (2019).

3 Neurohr, G. E. & Amon, A. Relevance and Regulation of Cell Density. *Trends Cell Biol* **30**, 213-225, doi:10.1016/j.tcb.2019.12.006 (2020).

4 Zhou, H. X., Rivas, G. & Minton, A. P. Macromolecular crowding and confinement: biochemical, biophysical, and potential physiological consequences. *Annu Rev Biophys* **37**, 375-397, doi:10.1146/annurev.biophys.37.032807.125817 (2008).

5 Son, S. *et al.* Resonant microchannel volume and mass measurements show that suspended cells swell during mitosis. *J Cell Biol* **211**, 757-763, doi:10.1083/jcb.201505058 (2015).

6 Zlotek-Zlotkiewicz, E., Monnier, S., Cappello, G., Le Berre, M. & Piel, M. Optical volume and mass measurements show that mammalian cells swell during mitosis. *J Cell Biol* **211**, 765-774, doi:10.1083/jcb.201505056 (2015).

7 Rojas, E. R. & Huang, K. C. Regulation of microbial growth by turgor pressure. *Curr Opin Microbiol* **42**, 62-70, doi:10.1016/j.mib.2017.10.015 (2018).

8 Neurohr, G. E. *et al.* Excessive Cell Growth Causes Cytoplasm Dilution And Contributes to Senescence. *Cell* **176**, 1083-1097.e1018, doi:10.1016/j.cell.2019.01.018 (2019).

9 Knapp, B. D. *et al.* Decoupling of Rates of Protein Synthesis from Cell Expansion Leads to Supergrowth. *Cell Syst* **9**, 434-445.e436, doi:10.1016/j.cels.2019.10.001 (2019).

10 Zangle, T. A. & Teitell, M. A. Live-cell mass profiling: an emerging approach in quantitative biophysics. *Nat Methods* **11**, 1221-1228, doi:10.1038/nmeth.3175 (2014).

11 Burg, T. P. *et al.* Weighing of biomolecules, single cells and single nanoparticles in fluid. *Nature* **446**, 1066-1069, doi:10.1038/nature05741 (2007).

12 Park, Y., Depeursinge, C. & Popescu, G. Quantitative phase imaging in biomedicine. *Nature Photonics* **12**, 578-589, doi:10.1038/s41566-018-0253-x (2018).

13 Lee, K. *et al.* Quantitative phase imaging techniques for the study of cell pathophysiology: from principles to applications. *Sensors (Basel, Switzerland)* **13**, 4170-4191, doi:10.3390/s130404170 (2013).

14 Bostan, E., Froustey, E., Nilchian, M., Sage, D. & Unser, M. Variational Phase Imaging Using the Transport-of-Intensity Equation. *IEEE Trans Image Process* **25**, 807-817, doi:10.1109/TIP.2015.2509249 (2016).

15 Mitchison, J. M. & Nurse, P. Growth in cell length in the fission yeast Schizosaccharomyces pombe. *J Cell Sci* **75**, 357-376 (1985).

16 Rappaz, B. *et al.* Noninvasive characterization of the fission yeast cell cycle by monitoring dry mass with digital holographic microscopy. *J Biomed Opt* **14**, 034049, doi:10.1117/1.3147385 (2009).

17 Atilgan, E., Magidson, V., Khodjakov, A. & Chang, F. Morphogenesis of the Fission Yeast Cell through Cell Wall Expansion. *Curr Biol* **25**, 2150-2157, doi:10.1016/j.cub.2015.06.059 (2015).

18 Simanis, V. Pombe's thirteen – control of fission yeast cell division by the septation initiation network. *Journal of Cell Science* **128**, 1465, doi:10.1242/jcs.094821 (2015).

19 Ray, S. *et al.* The mitosis-to-interphase transition is coordinated by cross talk between the SIN and MOR pathways in Schizosaccharomyces pombe. *Journal of Cell Biology* **190**, 793-805, doi:10.1083/jcb.201002055 (2010).

20 Martin, S. G. & Arkowitz, R. A. Cell polarization in budding and fission yeasts. *FEMS Microbiology Reviews* **38**, 228-253, doi:10.1111/1574-6976.12055 (2014).

21 Nurse, P., Thuriaux, P. & Nasmyth, K. Genetic control of the cell division cycle in the fission yeast Schizosaccharomyces pombe. *Molecular and General Genetics MGG* **146**, 167-178, doi:10.1007/BF00268085 (1976).

22 Hagan, I. & Yanagida, M. Novel potential mitotic motor protein encoded by the fission yeast cut7+ gene. *Nature* **347**, 563-566, doi:10.1038/347563a0 (1990).

23 Minet, M., Nurse, P., Thuriaux, P. & Mitchison, J. M. Uncontrolled septation in a cell division cycle mutant of the fission yeast Schizosaccharomyces pombe. *J Bacteriol* **137**, 440-446, doi:10.1128/JB.137.1.440-446.1979 (1979).

24 Pan, K. Z., Saunders, T. E., Flor-Parra, I., Howard, M. & Chang, F. Cortical regulation of cell size by a sizer cdr2p. *eLife* **3**, e02040, doi:10.7554/eLife.02040 (2014).

25 Mutavchiev, D. R., Leda, M. & Sawin, K. E. Remodeling of the Fission Yeast Cdc42 Cell-Polarity Module via the Sty1 p38 Stress-Activated Protein Kinase Pathway. *Current biology : CB* **26**, 2921-2928, doi:10.1016/j.cub.2016.08.048 (2016).

26 Muñoz, J. *et al.* Extracellular cell wall β(1,3)glucan is required to couple septation to actomyosin ring contraction. *The Journal of cell biology* **203**, 265-282, doi:10.1083/jcb.201304132 (2013).

27 Berlin, A., Paoletti, A. & Chang, F. Mid2p stabilizes septin rings during cytokinesis in fission yeast. *J Cell Biol* **160**, 1083-1092, doi:10.1083/jcb.200212016 (2003).

28 Bryan, A. K., Goranov, A., Amon, A. & Manalis, S. R. Measurement of mass, density, and volume during the cell cycle of yeast. *Proc Natl Acad Sci U S A* **107**, 999-1004, doi:10.1073/pnas.0901851107 (2010).

29 Mitchison, J. M. The growth of single cells. I. Schizosaccharomyces pombe. *Exp Cell Res* **13**, 244-262, doi:10.1016/0014-4827(57)90005-8 (1957).

30 Stonyte, V., Boye, E. & Grallert, B. Regulation of global translation during the cell cycle. *J Cell Sci* **131**, doi:10.1242/jcs.220327 (2018).

31 Godin, M. *et al.* Using buoyant mass to measure the growth of single cells. *Nat Methods* **7**, 387-390, doi:10.1038/nmeth.1452 (2010).

32 Liu, X., Oh, S., Peshkin, L. & Kirschner, M. W. Computationally Enhanced Quantitative Phase Microscopy Reveals Autonomous Oscillations in Mammalian Cell Growth. *bioRxiv*, 631119, doi:10.1101/631119 (2019).

33 Miettinen, T. P., Kang, J. H., Yang, L. F. & Manalis, S. R. Mammalian cell growth dynamics in mitosis. *Elife* **8**, doi:10.7554/eLife.44700 (2019).

34 Oldewurtel, E. R., Kitahara, Y., Cordier, B., Özbaykal, G. & van Teeffelen, S. Bacteria control cell volume by coupling cell-surface expansion to dry-mass growth. *bioRxiv*, 769786, doi:10.1101/769786 (2019).

35 Harding, C. V. & Feldherr, C. Semipermeability of the nuclear membrane in the intact cell. *J Gen Physiol* **42**, 1155-1165, doi:10.1085/jgp.42.6.1155 (1959).

36 Edelstein, A. D. *et al.* Advanced methods of microscope control using μManager software. *J Biol Methods* **1**, doi:10.14440/jbm.2014.36 (2014).

37 Ursell, T. *et al.* Rapid, precise quantification of bacterial cellular dimensions across a genomic-scale knockout library. *BMC Biol* **15**, 17, doi:10.1186/s12915-017-0348-8 (2017).

38 Grover, W. H. *et al.* Measuring single-cell density. *Proc Natl Acad Sci U S A* **108**, 10992-10996, doi:10.1073/pnas.1104651108 (2011).

39 Kang, J. H. *et al.* Noninvasive monitoring of single-cell mechanics by acoustic scattering. *Nat Methods* **16**, 263-269, doi:10.1038/s41592-019-0326-x (2019).

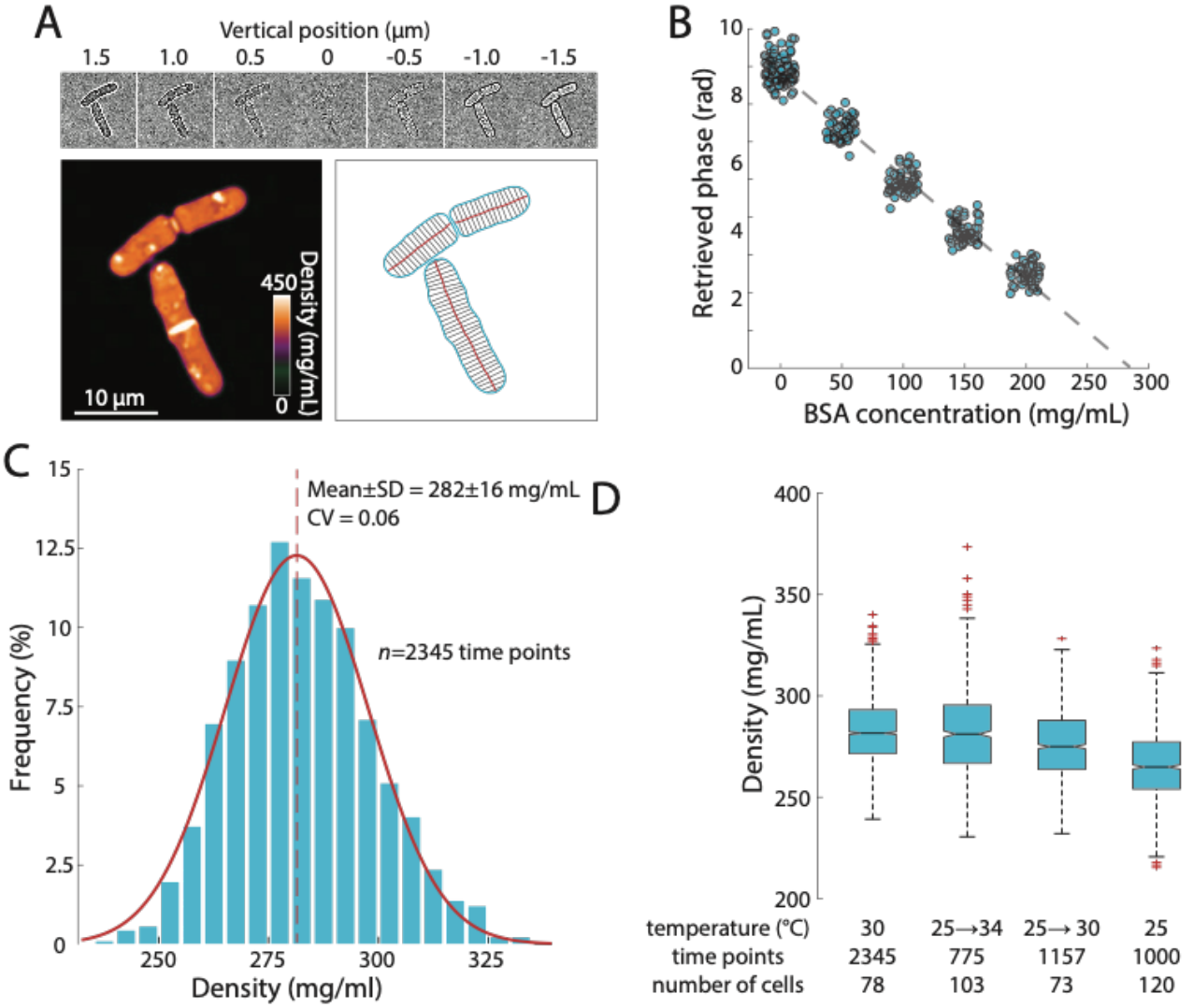

Figure 1: Precise measurement of intracellular density using quantitative phase imaging (QPI) based on a *z*-stack of brightfield images.

A) QPI method for computing cytoplasmic density from brightfield images. A *z*-stack of brightfield images of fission yeast cells ±1.5 μm around the focal position (top) were computationally analyzed by solving the transport-of-intensity equation to retrieve pixel-by-pixel phase-shift maps (bottom left). Cellular dimensions were determined via segmentation and skeletonization (bottom right).

B) QPI phase shifts were calibrated by imaging cells in medium supplemented with a range of concentrations of BSA. The retrieved phase shift is linearly related to concentration.

C) Histogram of dry-mass density measurements of exponential-phase fission yeast cells grown at 30 °C in YE5S medium. A Gaussian fit (red) yielded a mean density of 282±16 mg/mL (*n*=2345 time points, 78 cells).

D) Average cell density varied by less than 10% across different temperatures and temperature shifts.

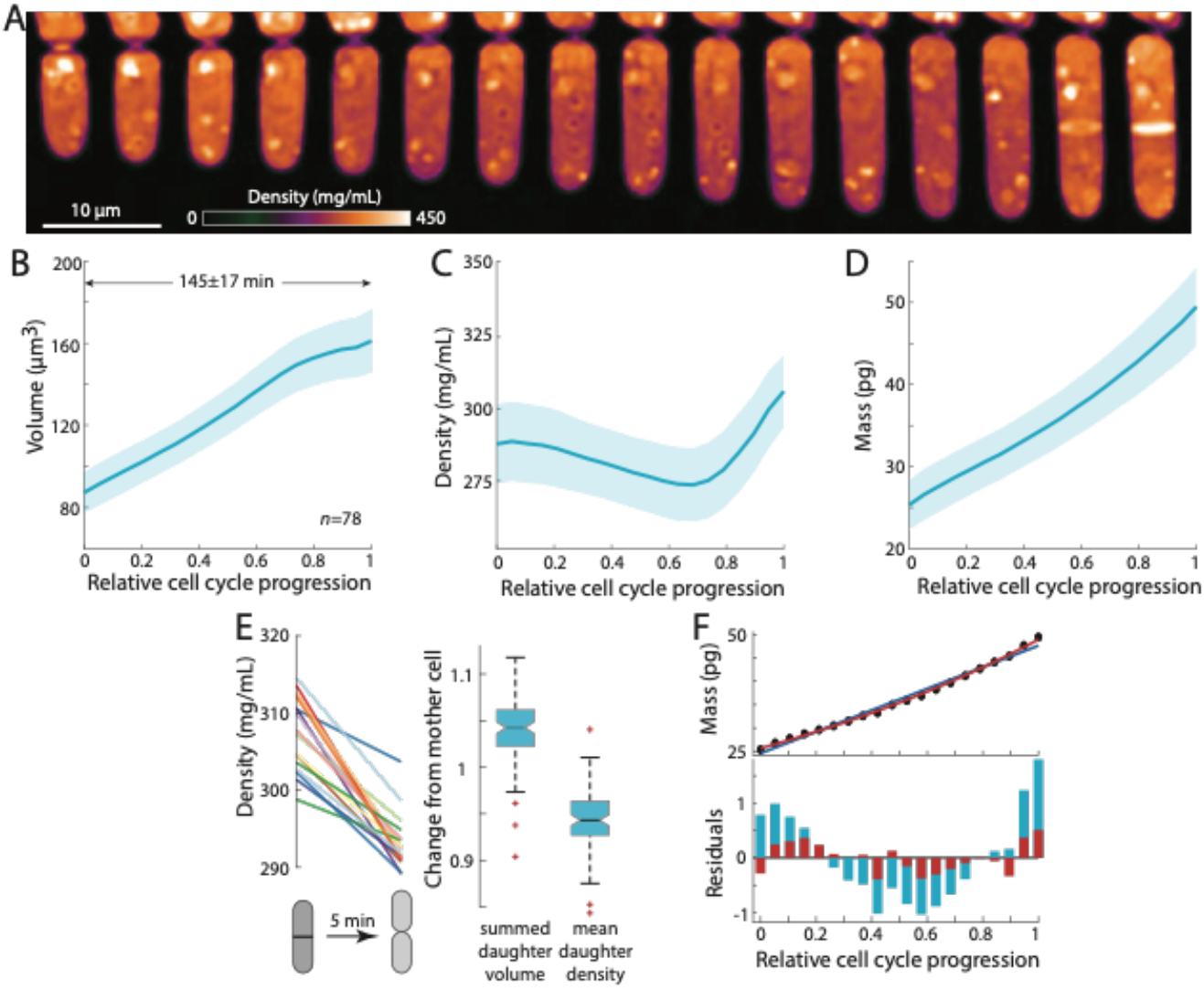

Figure 2: Intracellular density varies across the cell cycle.

A) Wild-type fission yeast cells in exponential phase were imaged in time lapse in a microfluidic chamber and phase-shift maps were extracted by QPI. Shown are images of a representative cell traversing the cell cycle from cell birth to septation (10 min/frame).

B-D) Cell volume (B), density (C), and dry mass (D) of cells aligned by their relative progression in the cell cycle. Curves are mean values and shaded regions represent 1 standard deviation (SD) (n=78 cells). Mass was estimated from volume and density measurements.

E) Cell density decreases upon cell separation. During the 5 min directly after cell separation, the summed volume of the daughter cells increased by ~5% while the average density of the daughter cells decreased by ~5%.

F) Dry mass grows exponentially. The residuals of an exponential fit (red) to mass growth were much smaller than a linear fit (blue).

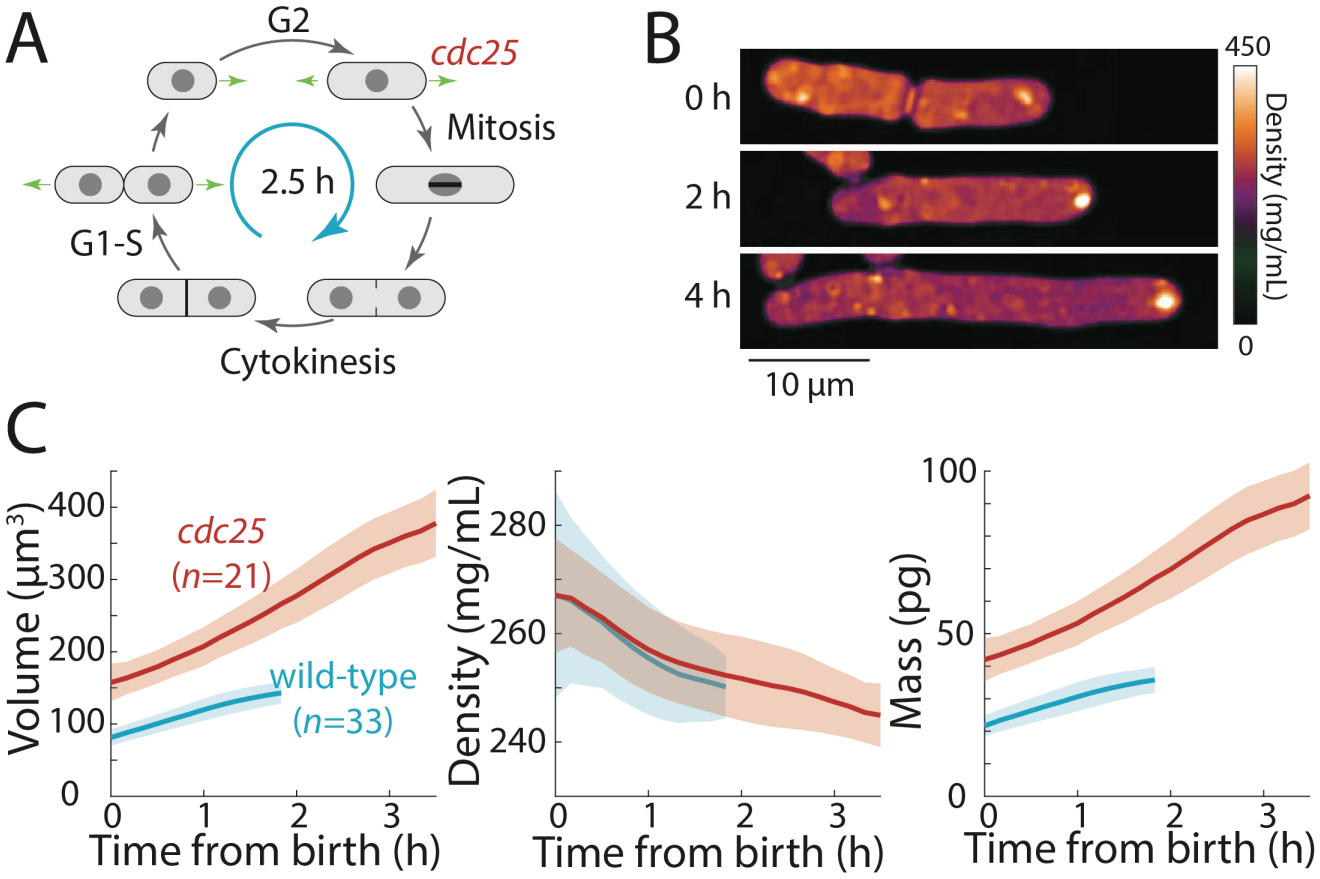

Figure 3: Extension of G2-phase cell cycle stage results in cell elongation and decreased intracellular density.

A) Schematic of fission yeast cell cycle, highlighting the point at which a *cdc25* temperature-sensitive mutant was to delay progression to mitosis.

B) *cdc25-22* cells were shifted from the permissive temperature 25 °C to the semi-permissive temperature 32 °C to extend G2 phase, leading to continued cell elongation. QPI images of a representative cell are shown.

C) Volume (left), density (middle), and dry mass (right) measurements of *cdc25-22* cells that grew at least 2.5-fold relative to their birth length before dividing, compared with wild-type cells under same conditions. Measurements are aligned from cell birth until elongation rate decreased to 20 nm/min (as an indication of the transition to mitosis).

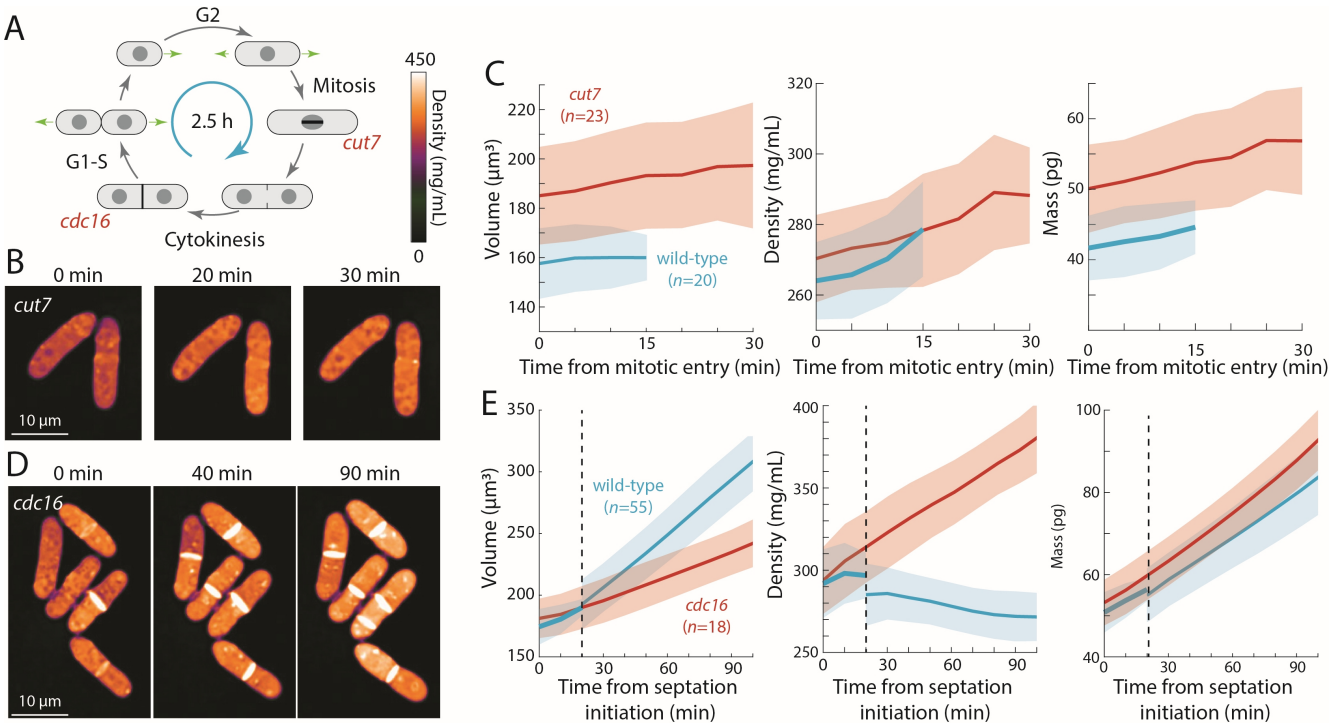

Figure 4: Cell cycle arrests in mitosis and cytokinesis result in increased intracellular density.

A) Schematic indicating stages of cell cycle blocks induced by temperature-sensitive mutants *cut7-446* (spindle kinesin-5) and *cdc16-116.*

B) *cut7-446* cells were shifted from 25 °C to 30 °C to delay mitotic progression. QPI images of two representative cells delayed in mitosis for ~20 min until the onset of septation (30 min time point).

C) Volume (left), density (middle), and dry mass (right) measurements of *cut7-446* cells from mitotic entry (t=0) through initiation of septum formation at cytokinesis. Density continued to increase during mitotic arrest.

D) *cdc16-116* cells were shifted from 25 °C to 34 °C to arrest cells in cytokinesis. QPI images of five representative cells are shown. *cdc16* cells generally did not complete cell separation and often assembled additional septa without elongating.

E) Volume (left), density (middle), and dry mass (right) measurements of *cdc16-116* cells from initiation of the first septum (t=0). Wild-type cells separated after ~20 min (dashed line), and thereafter the behavior of the daughter cells was tracked for comparison with *cdc16* cells (volume and dry mass were summed for the two daughter cells). Density increased during cytokinetic arrest.

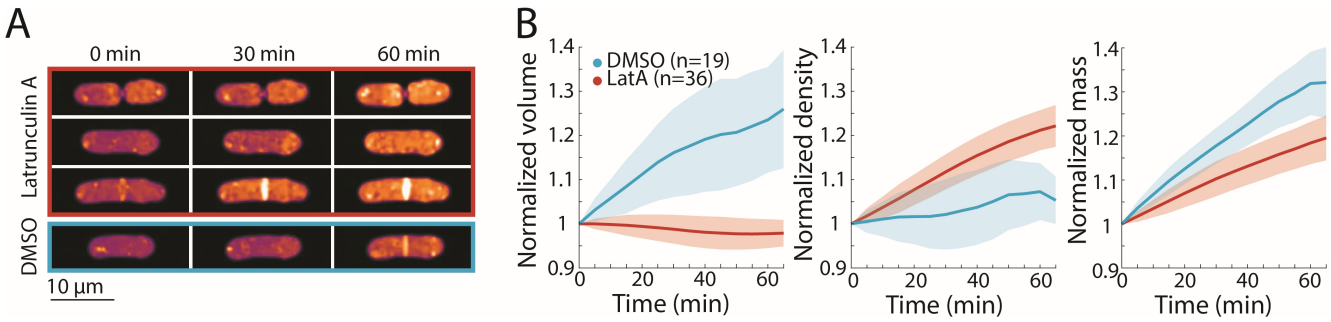

Figure 5: Cell cycle-independent growth inhibition by Latrunculin A results in increased intracellular density.

A) Latrunculin A inhibited cell growth and cell cycle progression regardless of cell-cycle stage. Representative images of wild-type cells treated with 0.2 mM latrunculin A at different cell cycle stages (shortly after division, during interphase, and during cytokinesis), each at 0, 30, or 60 min after the start of treatment. As a control (bottom), cells were treated with the equivalent amount of DMSO (1 µL/100 µL YE+agarose); growth continued and density remained relatively constant.

B) Volume (left), density (middle), and dry mass (right) measurements of latrunculin A-treated wild-type cells from the start of treatment (t=0). Growth halted and density increased due to continued mass synthesis during treatment.

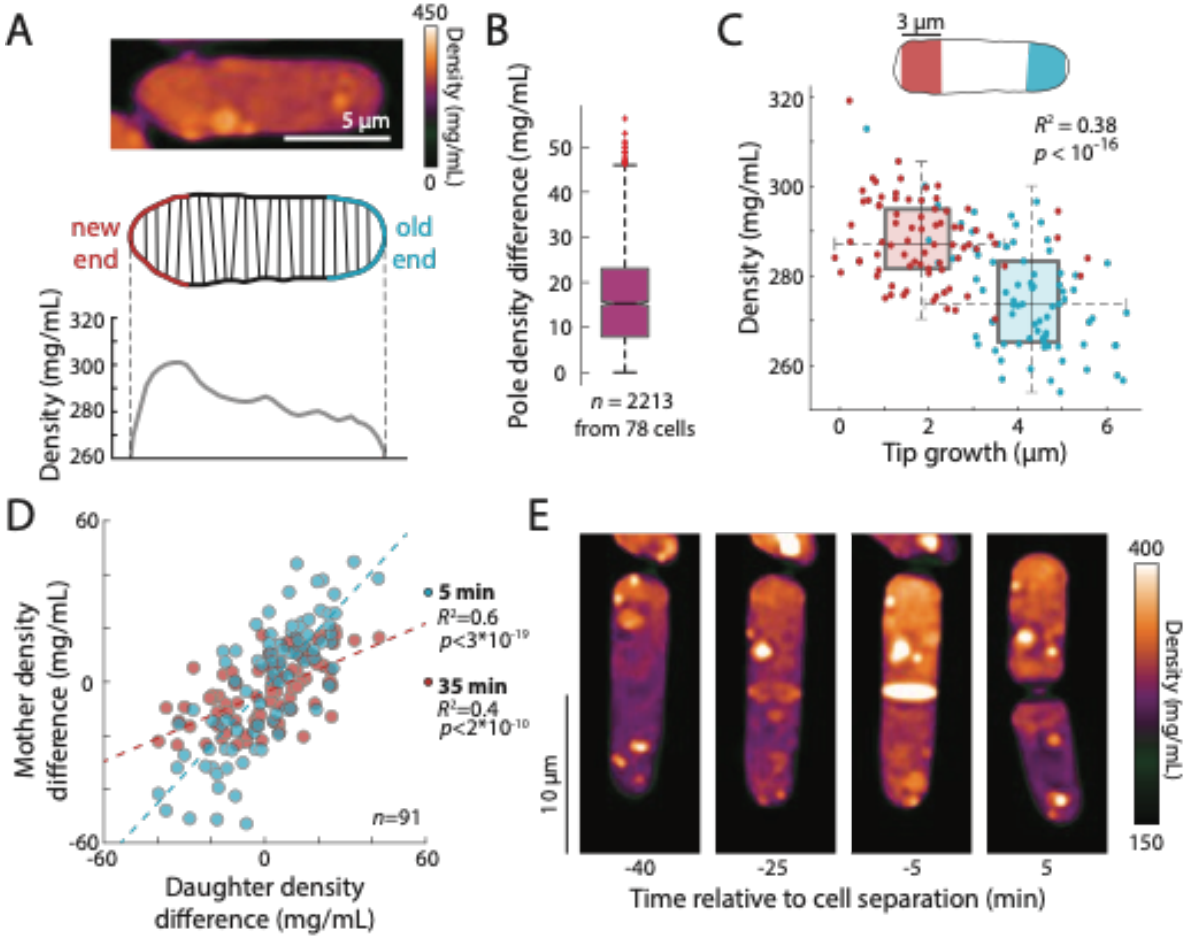

Figure 6: An intracellular density gradient negatively correlates with tip growth.

A) Top: QPI image of a representative cell displaying an intracellular gradient of density. Middle: density was measured in slices perpendicular to the long axis. Bottom: the new end (non- or slowly growing) exhibited a higher density than the old (growing) end.

B) Density was substantially different between the new and old ends in many cells. Time-lapse QPI images were used to measure the densities in regions within 3 µm of each cell end. Shown is the density difference between the cell poles averaged over the cell cycle. Box extends from 25th to 75th percentile, with the median as a horizontal bar. Whiskers indicate extreme points not considered outliers (n=78 cells).

C) Old ends grew more and exhibited lower mean densities over the course of the cell cycle than new ends.

D) Correlation between the density difference of daughter cells and the corresponding halves of the mother cell at 5 min (blue) or 35 min (red) before cell division. The halves of the mother cell exhibited larger density differences at the later time point, consistent with the density differences between daughter cells.

E) QPI images of a representative cell at interphase, start of septum formation, late in septum formation, and after cell division. The gradient in the interphase cell was maintained over time and passed on to the daughter cells.

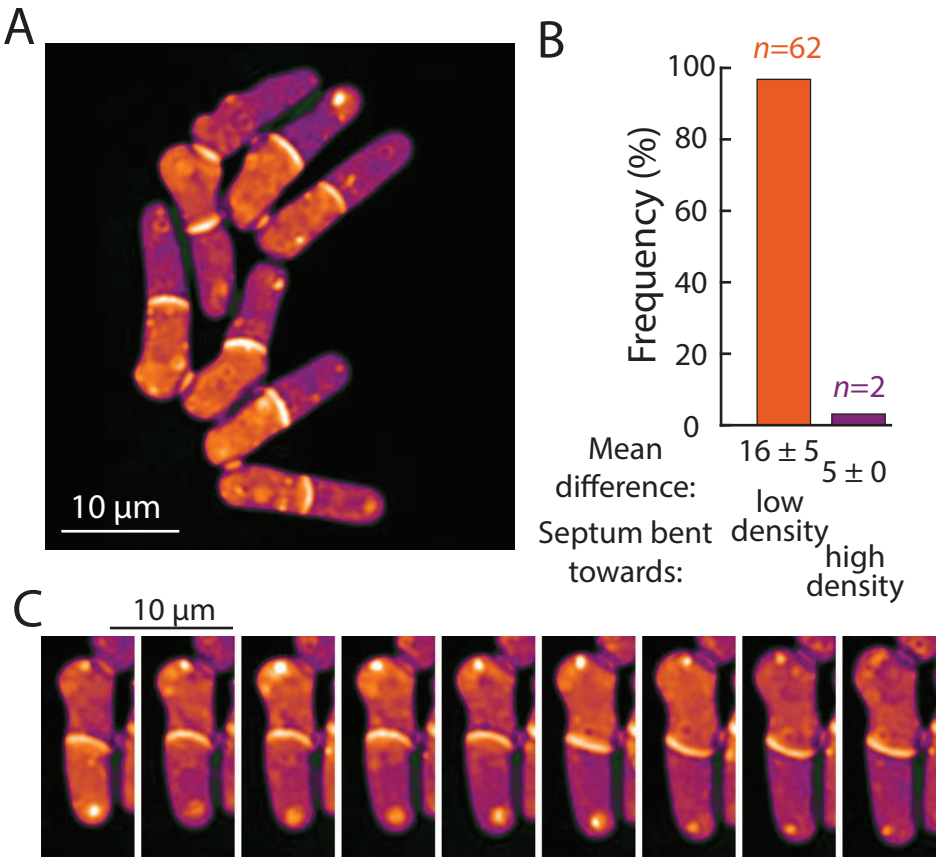

Figure 7: Bending of the septum reveals a correlation between intracellular density and osmotic pressure.

A) Representative image showing bent septa and density differences between the two daughter-cell compartments after cytokinesis.

B) In 62 of 64 cells with a bent septum at the time point of maximum density difference between daughter-cell compartments, the septum was bent away from the higher-density compartment, with a higher density difference than in the 2 cells in which the septum was bent toward the higher-density compartment.

C) An example cell in which the direction of septal bending and the sign of the density difference between daughter-cell compartments fluctuated over time (5 min/frame). After the bottom compartment decreased and the top compartment increased in density, the septum bent in the opposite direction, consistent with the correlation between bending and density difference in (B).

Supplemental Table

Table S1: *S. pombe* strains used in this study.

h- wild-type (972)	FC15
h- cdc25-22	FC342
h- cut7-446 leu1-32	FC1455
h- cdc16-116	FC13
h- mid2::kanMX ade6 leu1-32 ura4-D18	FC881

Supplemental Figures

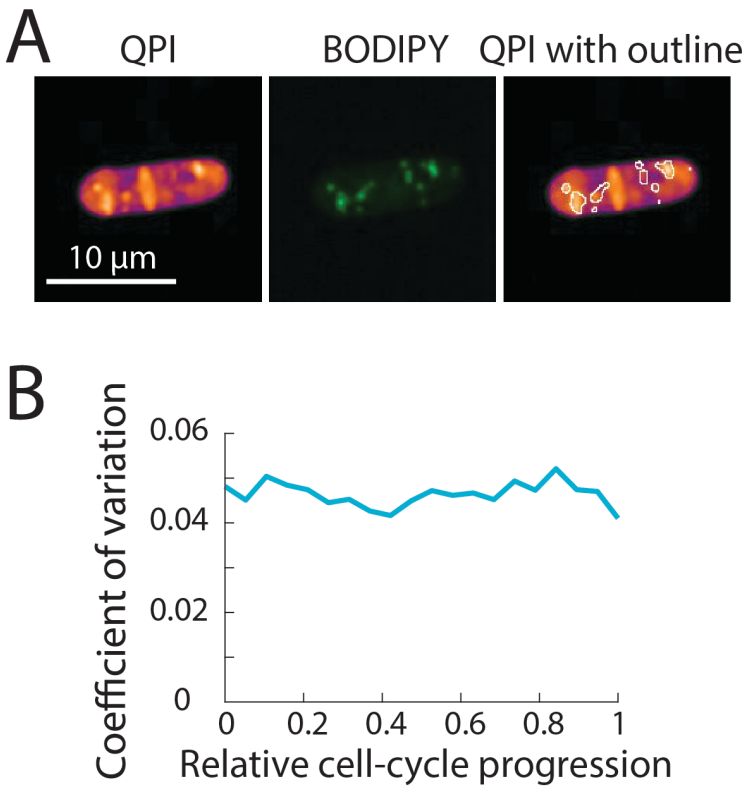

Supplemental Figure 1: High-density features in QPI images co-localize with lipid droplets.

A) QPI image (left) and corresponding fluorescence image of a representative BODIPY-stained wild-type cell (middle). The fluorescence intensity image was thresholded to identify regions containing lipid droplets, which overlapped with high-density regions of the QPI image (right).

B) Coefficient of variation (CV) of intracellular density over the cell cycle. The CV at each specific stage of cell-cycle progression (<5%) was slightly lower compared with the CV across an entire cell population (6%, Figure 1C), supporting the notion that some population-wide variation arises from cell-cycle dependent density variations.

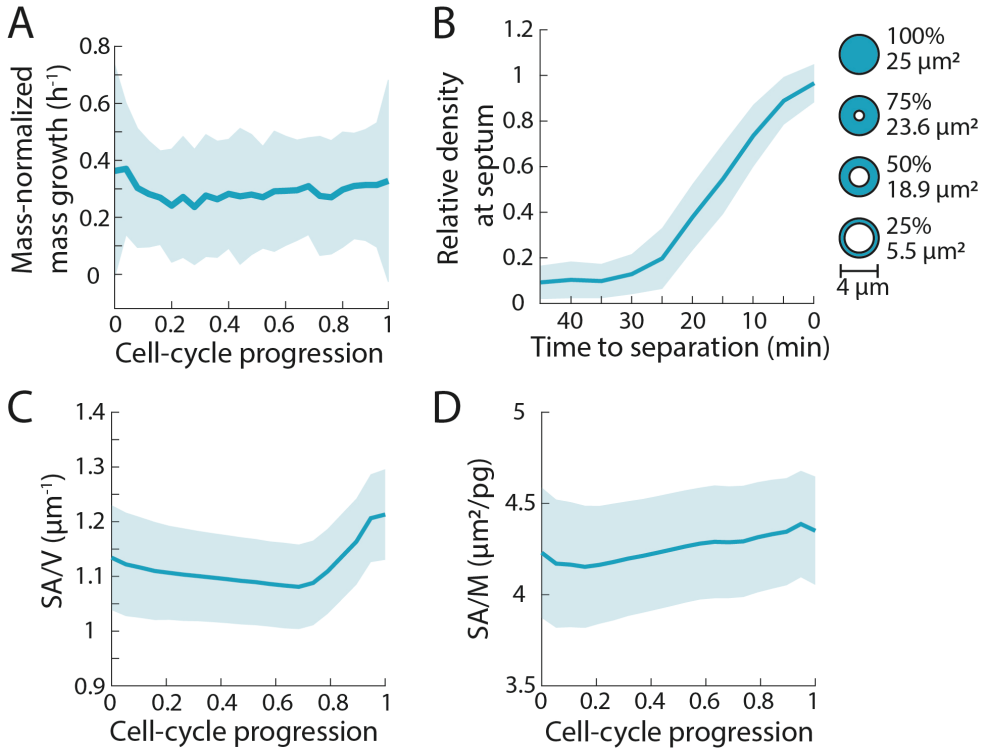

Supplemental Figure 2: Surface area to mass ratio varies less than dry-mass density during the cell cycle.

A) Mass growth normalized by cell mass ($1/M\ dM/dt$) remained relatively constant throughout the cell cycle; larger cells added more mass per unit time, a characteristic of exponential mass growth.

B) An estimate of septum growth by measurement of density at the septal region prior to division. The area of the septum was calculated by assuming a double-layered structure with a diameter of 4 µm. The intensity was used to estimate the diameter of the opening, such that at 50% intensity, 50% of the cross-sectional diameter was assumed to be filled.

C) Surface area to volume (SA/V) ratio increased at the end of the cell cycle, as volume growth slowed down and surface area increased due to septum formation.

D) Surface area to mass (SA/M) ratio varied by only ~5%.

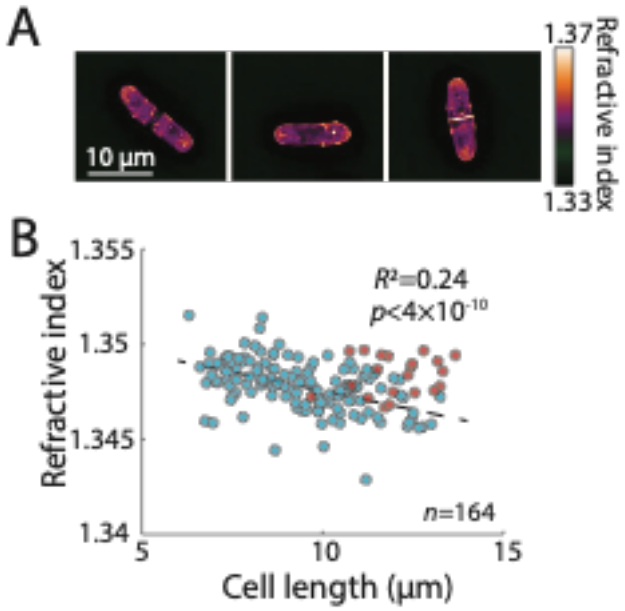

Supplemental Figure 3: Refractive index measurements based on holography show cell cycle-dependent density variation.

A) Representative holographic images of cells at an early, middle, and late stage in the cell cycle.

B) The mean refractive index was calculated from holographic images of non-septated cells (blue) and septated cells (red). The negative correlation for non-septated cells (dashed line) indicates that refractive index decreases with increasing cell length.

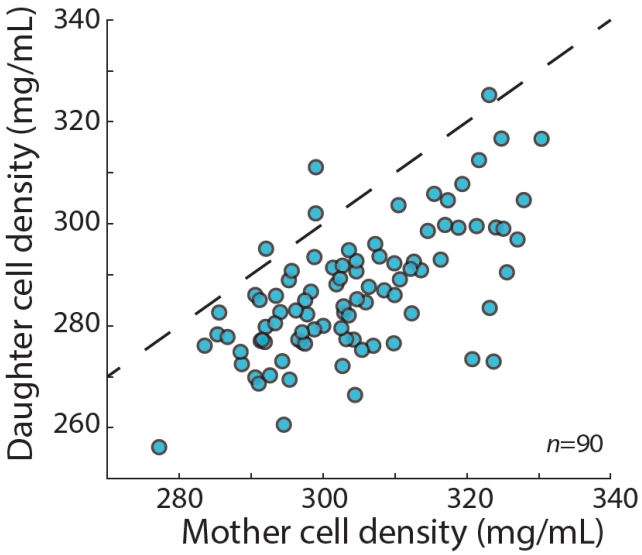

745

746 **Supplemental Figure 4: The mean density of daughter cells was typically lower than that**
747 **of the mother cell.**
748 Mean density of mother cell and daughter cells were measured from consecutive images (5 min
749 apart) directly before and after cell division, respectively. The daughter cell densities were then
750 averaged.

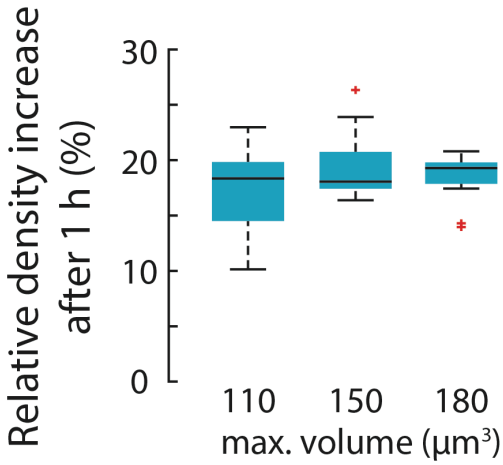

Supplemental Figure 5: The increase in intracellular density due to treatment with the actin inhibitor latrunculin A was not dependent on cell size.

Cells were treated for 1 h with 0.2 mM latrunculin A as described in Figure 6. Relative density increases per cell were plotted according to cell size. (Cells per bin: 10, 10, 12).

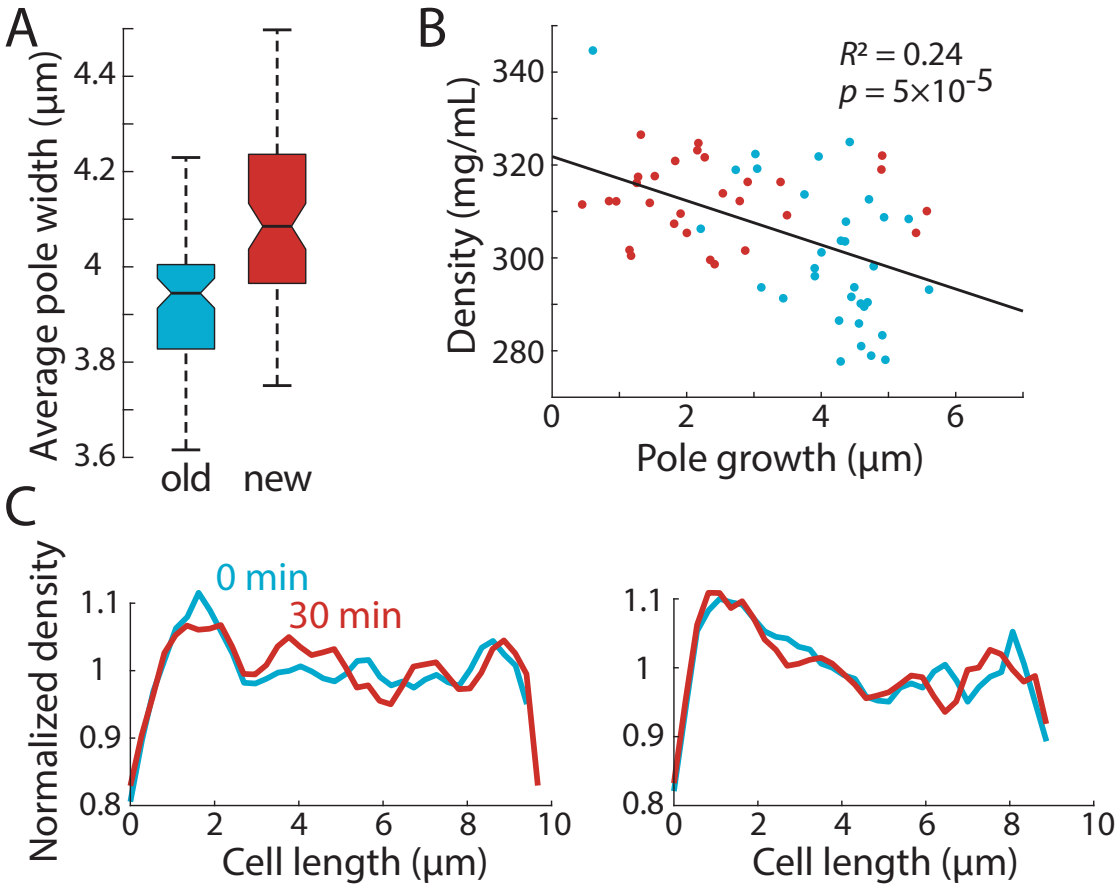

Supplemental Figure 6: Spatial intracellular density gradients in cells with similar widths, and in cells treated with Latrunculin A.

A) The mean width of the region between 1.5-3 μm away from the cell pole was extracted for the new and old pole over time and averaged. The average old pole width was ~0.15 μm smaller than that of new poles.

B) To correct for potential height-related effects on intracellular density measurements, we constrained our measurements of average pole density to new and old poles with width between 3.9 and 4.1 μm (corresponding to the medians in (A)). The negative correlation between pole growth and density observed in Figure 3C persisted, suggesting that the difference in measured density between poles is not an QPI artifact due to differences in sample height.

C) Stability of the density gradient in Latrunculin A-treated cells. Normalized density plots along the length of individual cells before and 30 min after treatment with Latrunculin A. The gradient-like distribution of density was maintained in these cells in the absence of F-actin and tip growth.

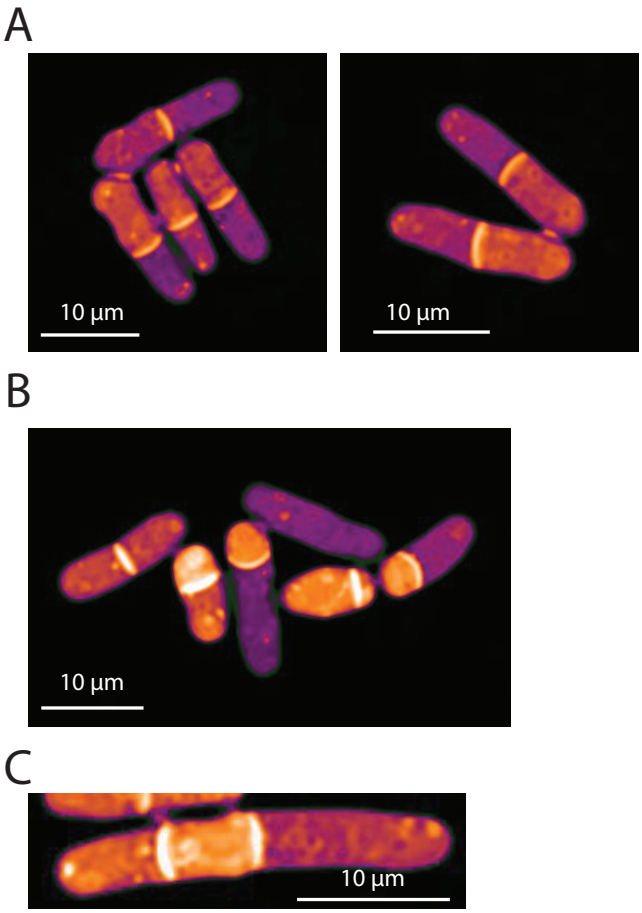

Supplemental Figure 7: Septa bend away from the compartment of higher density in *mid2* and *cdc16* mutant cells.

A) *mid2* cells with bent septa typically exhibited differences in density between sister-cell compartments, and in each case the septum was bent away from the compartment of higher density.

B) In *cdc16* cells, the septum was often located to one side of the middle of the cell, resulting in a small, higher-density compartment that failed to grow and a larger compartment of lower density that exhibited tip growth prior to cytokinesis.

C) In multi-septated *mid2Δ* cells, internal compartments bounded by two septa exhibited higher density than the surrounding compartments; in these situations, both septa typically bent away from the higher-density compartment.